Communication

An Accelerated Method of a Generalized Transition Matrix Model Using Characteristic Basis Functions for Large-Scale Open-Ended Cavities

Inhwan Kim, Hyeong-Rae Im, Ic-Pyo Hong, Hyunsoo Lee, and Jong-Gwan Yook

***Abstract*— This communication proposes a novel method for electrically large-scale open-ended cavities, using the generalized transition matrix (GTM) model and accelerating it by implementing the characteristic basis function method (CBFM). The approach involves the representation of electric surface currents on both the exterior and interior walls of a cavity using characteristic basis functions (CBFs), effectively reducing the number of unknowns in the problem. The proposed method can efficiently enhance the computational complexity of the GTM model construction as well as the system matrix formulation. Consequently, the system matrix is reduced compared with the original matrix system, resulting in the reduction of the matrix-solving times. The detailed formulation processes are introduced in this communication. Furthermore, the proposed method is verified using examples of open-ended cavities and evaluates the computational efficiency compared with the original method through the numerical results.**

***Index Terms*— Characteristic basis function methods (CBFMs), generalized transition matrix (GTM), method of moments (MoMs), open-ended cavity.**

I. Introduction

Open-ended cavities are common structures in both industrial and mechanical applications, serving as essential components in antennas, radar systems, or microwave circuits. In addition, these cavities are also employed for mechanical purposes such as engine inlets, intakes, and air-flow ducts for aerial vehicles. It is important to analyze and understand their electromagnetic phenomena and characteristics, including antenna patterns, gains, and radar cross section (RCS) of the structure [1], [2], [3], [4]. These analyses are complicated by the multiple reflections and complex interactions between the sources and internal structures.

To accurately analyze the electromagnetic characteristics of these cavities, conventional numerical methods can be used, such as the method of moments (MoMs) [5] and the finite-element method (FEM) [6]. While these methods provide precise solutions, they are less efficient for handling large-scale problems due to their computational complexity. Consequently, various alternative methods have been developed, including iterative physical optics (IPOs) in high-frequency approximations [7], [8], [9], hybrid methods [10], [11], [12], [13], and the domain decomposition method (DDM) [14].

In [7], [8], and [9], IPO was introduced to solve the problems for open-ended cavities, in which the electric currents are updated using the magnetic field integral equation to consider the multiple reflections within the cavity structure. Accordingly, several hybrid methods have been developed: [10] combined finite-element (FE)-boundary integral (BI) (FE-BI) with the multilevel fast multipole method (MLFMM), and [11] combined FE-BI with DDM. Recently, researches that divided cavities into interior and exterior regions while simultaneously considering the coupling between them [15] and [16]. Herein, we focus on the generalized transition matrix (GTM) model [15] which is an efficient method that simultaneously considers the interaction between the interior and exterior regions through an equivalent source on the apertures of the cavities and the field transmission matrix [17], [18]. However, although it is suitable for solving the open-ended cavity problem, the computational complexity increases as the physical dimensions or the target frequency increases.

The characteristic basis function method (CBFM) [19], [20], [21], [22] is a representative of numerical methods for solving electrically large-scale problems, which are based on the direct solver. The methods based on the direct solver do not suffer the convergence problem depending on the physical structures of problems. Additionally, they do not have computational degradations when solving multiple-excitation problems. Therefore, CBFM is particularly advantageous for monostatic RCS analysis. In this study, we employ CBFM to efficiently solve the electrically large-scale problems of open-ended cavities while continuing our previous work [23]. By leveraging characteristic basis functions (CBFs) to reduce the number of unknowns, large-scale problems with open-ended cavities can be efficiently solved. The derivation using CBFs is introduced, and the performance of the proposed method is demonstrated through the results of a numerical experiment.

The remainder of this communication is organized as follows. Section II provides a detailed discussion of the theories related to the GTM model and the CBFM. Section III introduces the formulation of the GTM model with CBFs and describes the reduced system matrix. In Section IV presents the numerical results of some open-ended cavities are discussed, followed by the conclusion in Section V.

II. Theoretical Review of GTM Model

The open-ended cavity can be separated into the interior and exterior regions, as shown in Fig. 1. The boundary between the interior and exterior regions is defined by a reference surface on which auxiliary sources are considered in accordance with Huygens's principle. Notably, this reference surface is a fictitious boundary that does not exist. In addition, the cavity consists of only perfect electric conductors, not any other materials. Therefore, only electric sources are considered on the surface of the cavity. However, it should be noted that both electric and magnetic sources exist on the reference surface. All sources which have to be considered are illustrated in Fig. 1.

The whole geometry is partitioned into the exterior and interior regions by defining the reference surface, where the junction serves as the connection between the two regions. It should be noted that the original junction current (J_q) is decomposed into the outer and inner

Manuscript received 22 November 2023; revised 30 April 2024; accepted 22 May 2024. Date of publication 5 June 2024; date of current version 9 August 2024. This work was supported by the Agency for Defense Development Grant Funded by the Korean Government under Grant UD230016JD. *(Corresponding author: Jong-Gwan Yook.)*

Inhwan Kim, Hyeong-Rae Im, and Jong-Gwan Yook are with the Department of Electrical and Electronic Engineering, Yonsei University, Seoul 03722, South Korea (e-mail: ih.kim@yonsei.ac.kr; ihr3021@yonsei.ac.kr; jgyook@yonsei.ac.kr).

Ic-Pyo Hong is with the Department of Information and Communication Engineering, Kongju National University, Cheonan 31080, South Korea (e-mail: iphong@kongju.ac.kr).

Hyunsoo Lee is with the Agency for Defense Development of the Republic of Korea, Daejeon 34186, South Korea.

Color versions of one or more figures in this article are available at https://doi.org/10.1109/TAP.2024.3407382.

Digital Object Identifier 10.1109/TAP.2024.3407382

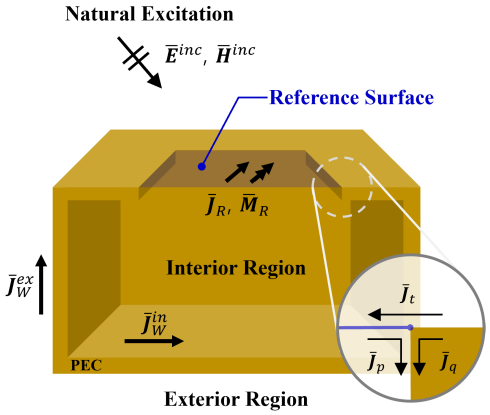

Fig. 1. Geometry and source distribution of the problem of the open-ended cavity problem. The space is divided into the exterior and interior regions by the reference surface located at the aperture of the cavity. The cavity considered in this communication consists of a perfectly electric conductor. The electric surface currents exist on the exterior, interior wall, and the junction, while both electric and magnetic surface currents exist on the reference surface.

junction, J_t and J_p, respectively. The inner and outer junctions are defined by sharing the identical domain, reference surface, on which the direction of the current is opposite to each other. Therefore, the continuities can be satisfied on both the auxiliary reference surface and original perfect electrical conductor (PEC) body [15]. The current on the outer junction is regarded as a source of the exterior fields, while the current on the inner junction is regarded as a source of the interior fields.

Note that the derivation procedure in this section follows the approach outlined in [15].

A. Construction of the GTM Model

Assuming that the cavity is lying in free space with no internal sources, the electric field $\vec{E}^{ex}(\vec{r})$ and the magnetic field $\vec{H}^{ex}(\vec{r})$ in the exterior region can be represented using the Huygens principle

$$\vec{E}^{ex}(\vec{r}) = -j\omega\mu\mathcal{L}\left(\vec{J}_R^{ex}\right) - \mathcal{K}\left(\vec{M}_R^{ex}\right) - j\omega\mu\mathcal{L}\left(\vec{J}_W^{ex}\right) + \vec{E}^{inc}(\vec{r}) \tag{1a}$$

$$\vec{H}^{ex}(\vec{r}) = -j\omega\epsilon\mathcal{L}\left(\vec{M}_R^{ex}\right) + \mathcal{K}\left(\vec{J}_R^{ex}\right) + \mathcal{K}\left(\vec{J}_W^{ex}\right) + \vec{H}^{inc}(\vec{r}) \tag{1b}$$

where

$$\left(\mathcal{L}\vec{X}\right)(\vec{r}) = \left\{1 + \frac{1}{k^2}\nabla\nabla\cdot\right\}\int_S G\left(\vec{r},\vec{r}'\right)\vec{X}\left(\vec{r}'\right)d\vec{r}' \tag{2a}$$

$$\left(\mathcal{K}\vec{X}\right)(\vec{r}) = \nabla\times\int_S G\left(\vec{r},\vec{r}'\right)\vec{X}\left(\vec{r}'\right)d\vec{r}' \tag{2b}$$

and $\vec{J}_R^{ex}$ and $\vec{M}_R^{ex}$ represent the fictitious sources on the reference surface in the exterior region, while $\vec{J}_W^{ex}$ correspond to the electric surface current on the exterior wall, $\vec{E}^{inc}(\vec{r})$ and $\vec{H}^{inc}(\vec{r})$ denote the incident fields originating from an excitation source. Accordingly, the electric field $\vec{E}^{in}(\vec{r})$ and the magnetic field $\vec{H}^{in}(\vec{r})$ in the interior region can be expressed as

$$\vec{E}^{in}(\vec{r}) = -j\omega\mu\mathcal{L}\left(\vec{J}_R^{in}\right) + \mathcal{K}\left(\vec{M}_R^{in}\right) - j\omega\mu\mathcal{L}\left(\vec{J}_W^{in}\right) - j\omega\mu\mathcal{L}\left(\vec{J}_p\right) \tag{3a}$$

$$\vec{H}^{in}(\vec{r}) = -j\omega\epsilon\mathcal{L}\left(\vec{M}_R^{in}\right) + \mathcal{K}\left(\vec{J}_R^{in}\right) + \mathcal{K}\left(\vec{J}_W^{in}\right) + \mathcal{K}\left(\vec{J}_p\right) \tag{3b}$$

where $\vec{J}_R^{in}$ and $\vec{M}_R^{in}$ represent the fictitious sources on the reference surface in the interior region, $\vec{J}_W^{in}$ corresponds to the electric surface current on the interior wall, and $\vec{J}_p$ corresponds to the electric surface current on the inner junction. First, the tangential components of both fields should be continuous on the reference surface under the following boundary conditions:

$$\vec{E}^{ex}(\vec{r})\Big|_{tan} = \vec{E}^{in}(\vec{r})\Big|_{tan} \tag{4a}$$

$$\vec{H}^{ex}(\vec{r})\Big|_{tan} = \vec{H}^{in}(\vec{r})\Big|_{tan} \tag{4b}$$

where $\vec{r} \in S_R$. In addition, since both electric and magnetic sources should be eliminated on the reference surface, the current sources in the interior and exterior regions have opposite signs: $\vec{J}_R^{ex} = -\vec{J}_R^{in}$ and $\vec{M}_R^{ex} = -\vec{M}_R^{in}$. Using the Rao–Wilton–Glisson (RWG) basis functions, (4) can be converted into a matrix equation using Galerkin's testing procedure [24]

$$\mathbb{Z}_R\cdot\mathbb{X}_R + \mathbb{A}\cdot\mathbb{J}_W^{in} + \mathbb{A}'\cdot\mathbb{J}_p = \mathbb{F}_R \tag{5}$$

where $\mathbb{Z}_R$ is the matrix calculated by testing the electromagnetic field on the reference surface from itself, $\mathbb{A}$ is the matrix calculated by testing the electromagnetic field on the reference surface from the electric current on the interior wall, and $\mathbb{A}'$ is the matrix a matrix calculated by testing the electromagnetic field on the reference surface from the electric current on the inner junction. $\mathbb{X}_R$ is a vector consisting of the expansion coefficients of $\vec{J}_R$ and $\vec{M}_R$, $\mathbb{J}_W^{in}$ and $\mathbb{J}_p$ are the expansion coefficients of J_W^{in} and J_p, respectively. Notably, $\mathbb{F}_R$ is a vector containing the expansion coefficients for not only $\vec{E}^{inc}$ and $\vec{H}^{inc}$ but also for all incoming incident fields to the interior region from the exterior region through the reference surface.

Second, to satisfy the PEC boundary condition, the tangential electric field on the interior wall should be eliminated

$$\vec{E}^{in}(\vec{r})\Big|_{tan} = 0 \quad \text{where } \vec{r} \in S_{in}. \tag{6}$$

Similarly, another matrix equation is obtained through Galerkin's testing procedure from (6)

$$\mathbb{B}\cdot\mathbb{J}_W^{in} + \mathbb{B}'\cdot\mathbb{J}_p + \mathbb{C}\cdot\mathbb{X}_R = 0 \tag{7}$$

where $\mathbb{B}$ is the matrix calculated by testing the electric field from the current on the interior wall, $\mathbb{B}'$ is the matrix calculated by testing the electric field from the current on the inner junction, and $\mathbb{C}$ is the matrix calculated by testing the electric field from the current on the reference surface [15]. By combining (5) and (7), and eliminating the term $\mathbb{J}_W^{in}$, the GTM model can be constructed as

$$\mathbb{X}_R = \mathbb{T}\cdot\mathbb{F}_R + \mathbb{M}_t\cdot\mathbb{J}_t \tag{8}$$

where $\mathbb{T} = (\mathbb{Z}_R - \mathbb{A}\mathbb{B}^{-1}\mathbb{C})^{-1}$, $\mathbb{M}_t = (\mathbb{Z}_R - \mathbb{A}\mathbb{B}^{-1}\mathbb{C})^{-1}(\mathbb{A}\mathbb{B}^{-1}\mathbb{B}' - \mathbb{A}')$, and the vector for the electric current on the inner junction ($\mathbb{J}_p$) is replaced by one for the outer junction ($\mathbb{J}_t$) [15]. It is noted that the fictitious sources can be reconstructed without simultaneous consideration of the interior region by using the GTM model.

Assuming that only one reference surface is considered, the incident fields on the surface can be represented as

$$\mathbb{F}_R = \mathbb{F}_R^{inc} + \mathbb{D}_{R0}\cdot\mathbb{J}_0 + \mathbb{D}_{Rt}\cdot\mathbb{J}_t \tag{9}$$

where 0 denotes the exterior wall, $\mathbb{D}_{R0}$ is the field transmission matrix from the exterior wall to the reference surface, and $\mathbb{D}_{Rt}$ is the field transmission matrix from the junction to the reference surface, which is represented as a summation of all interactions.

B. Matrix System Formulation With the GTM Model

To construct a linear system for the problem, the PEC boundary condition has to be enforced on the exterior wall and outer junction of the cavity. Using Galerkin's testing procedure, a linear system can be constructed using the GTM model

$$\mathbb{Z}_0 \cdot \mathbb{J}_0 = \mathbb{E}_0^{inc} + \mathbb{D}_{0R} \cdot \mathbb{X}_R + \mathbb{D}_{0t} \cdot \mathbb{J}_t \tag{11}$$

$$\mathbb{Z}_t \cdot \mathbb{J}_t = \mathbb{E}_t^{inc} + \mathbb{D}_{tR} \cdot \mathbb{X}_R + \mathbb{D}_{t0} \cdot \mathbb{J}_0 \tag{12}$$

where $\mathbb{Z}_0$ and $\mathbb{Z}_t$ are the impedance matrices calculated by testing the exterior wall and outer junctions, respectively, using the PEC boundary conditions. The matrices, $\mathbb{D}$ with subscripts, are defined as the field transmission matrices which can be calculated by testing the scattered fields on the observation surface from their sources [18]. The subscript 0 denotes the exterior wall, R denotes the reference surface, and t denotes the outer junction. Therefore, $\mathbb{D}_{0R}$ implies the field transmission from the reference surface to the exterior wall, and this same principle applies to the other matrices as well. The right-hand side vectors consist of fields transmitted from other sources. The first term represents the illuminated incident fields from the natural excitation, the second term denotes the fields transmitted from the GTM model, and the third term indicates the field transmitted from the outer junctions in (11) and from the exterior wall in (12). A solution to the problem can be obtained by solving (8), (9), (11), and (12).

III. Acceleration of the GTM Model Method Using CBFs

A. Characteristic Basis Function

The CBFM is a representative of numerical methods for solving electrically large-scale problems. In CBFM, the entire geometry is partitioned into multiple blocks, and CBFs are computed within each block [19] as shown in Fig. 2. The CBFs are calculated by solving the linear system of the blocks. The right-hand-side vectors in the equation comprise a combination of omnidirectional plane wave excitations

$$\mathbb{Z}_{CB}^i \cdot \mathbb{J}_{CB}^i = \mathbb{V}_{CB}^i \tag{13}$$

where $\mathbb{Z}_{CB}^i$ is the impedance matrix of the ith block and $\mathbb{V}_{CB}^i$ consists of columns that represent plane wave excitations. When calculating the CBFs, the blocks are extended by some portion to ensure continuity between adjacent blocks [19] as shown in Fig. 2. After the CBFs have been calculated for every block, the original solution vector can be expressed as a linear combination of the CBFs

$$\mathbb{J} = \sum_{i=1}^{M} \mathbb{J}_{CB}^i \cdot \alpha^i \tag{14}$$

where M is the number of blocks and $\mathbb{J}_{CB}^i$ are the CBFs of the ith block. The dimensions of $\mathbb{J}_{CB}^i$ and α^i are $N_{CB}^i \times N^i$ and $N^i \times 1$, respectively, where N_{CB}^i is the number of CBFs and N^i is the number of RWG basis functions in the ith block.

B. GTM Model Construction With Reduced Form of Matrices Using CBFs

The interior and exterior walls of the cavity are divided into subblocks, and the CBFs in each block are precalculated. The electric current on the interior and exterior walls of the cavity can be replaced by CBFs. As the number of CBFs is smaller than the number of the original RWG basis functions, the size of the matrices in the derivation can be reduced. The matrix $\mathbb{A}$ can be reduced as follows:

$$\tilde{\mathbb{A}} = \begin{bmatrix} \mathbb{A}_1 \cdot \mathbb{J}_{CB}^1 \\ \vdots \\ \mathbb{A}_i \cdot \mathbb{J}_{CB}^i \\ \vdots \\ \mathbb{A}_N \cdot \mathbb{J}_{CB}^N \end{bmatrix}^{\mathrm{T}} \tag{15}$$

where $\mathbb{A}_i$ is the submatrix of $\mathbb{A}$ and $\mathbb{J}_{CB}^i$ is the CBF of the ith block of the interior wall. N is the number of interior wall blocks. Therefore, the number of columns is reduced to the number of CBFs on the interior wall. Similarly, the size of the matrices $\mathbb{B}'$ and $\mathbb{C}$ can also be reduced.

Since the matrix, $\mathbb{B}$, is calculated by testing the surface current on the interior wall itself, the dimension of both columns and rows can be reduced as (10), shown at the bottom of the page, where $\mathbb{A}_{ij}$ is the submatrix of $\mathbb{A}$, which is an interaction impedance matrix from the jth block to ith block. Furthermore, $\mathbb{J}_{CB}^i$ is the CBF of the ith block of the interior wall. The dimensions of the rows and columns are changed by the number of CBFs on the interior wall. Also, note that interaction impedance matrices are calculated by using the adaptive-cross approximation (ACA) algorithm for further acceleration [25].

Consequently, the GTM can be constructed using the reduced forms of the matrices

$$\mathbb{T} = \left(\mathbb{Z}_R - \tilde{\mathbb{A}}\tilde{\mathbb{B}}^{-1}\tilde{\mathbb{C}}\right)^{-1} \tag{16a}$$

$$\mathbb{M}_t = \left(\mathbb{Z}_R - \tilde{\mathbb{A}}\tilde{\mathbb{B}}^{-1}\tilde{\mathbb{C}}\right)^{-1}\left(\tilde{\mathbb{A}}\tilde{\mathbb{B}}^{-1}\tilde{\mathbb{B}}' - \tilde{\mathbb{A}}'\right) \tag{16b}$$

where the matrices, $\tilde{\mathbb{A}}$, $\tilde{\mathbb{A}}'$, $\tilde{\mathbb{B}}$, $\tilde{\mathbb{B}}'$, and $\tilde{\mathbb{C}}$, are the reduced form of $\mathbb{A}$, $\mathbb{A}'$, $\mathbb{B}$, $\mathbb{B}'$, and $\mathbb{C}$. Since the equations of the GTM model involve the matrix inversion, which increases computational complexity, the reduced forms of the matrices can provide computational efficiency for constructing the model.

C. System Matrix Formulation With GTM Model Using CBFs

Accordingly, the original linear system of the cavity with the GTM can be reduced using the reduced form of the matrices. Similarly, the matrices ($\mathbb{Z}_0$, $\mathbb{D}_{0R}$, $\mathbb{D}_{0t}$) in (11) can be reduced using the CBFs of the electric current on the exterior wall. The reduced linear system can be represented as

$$\tilde{\mathbb{Z}}_0 \cdot \tilde{\mathbb{J}}_0 = \tilde{\mathbb{E}}_0^{inc} + \tilde{\mathbb{D}}_{0R} \cdot \mathbb{X}_R + \tilde{\mathbb{D}}_{0t} \cdot \mathbb{J}_t \tag{17}$$

$$\tilde{\mathbb{B}} = \begin{bmatrix} \left(\mathbb{J}_{CB}^1\right)^T \cdot \mathbb{A}_{11} \cdot \mathbb{J}_{CB}^1 & \cdots & \left(\mathbb{J}_{CB}^1\right)^T \cdot \mathbb{A}_{1j} \cdot \mathbb{J}_{CB}^j & \cdots & \left(\mathbb{J}_{CB}^1\right)^T \cdot \mathbb{A}_{1N} \cdot \mathbb{J}_{CB}^N \\ \vdots & \ddots & \vdots & \ddots & \vdots \\ \left(\mathbb{J}_{CB}^i\right)^T \cdot \mathbb{A}_{i1} \cdot \mathbb{J}_{CB}^1 & \cdots & \left(\mathbb{J}_{CB}^i\right)^T \cdot \mathbb{A}_{ij} \cdot \mathbb{J}_{CB}^j & \cdots & \left(\mathbb{J}_{CB}^i\right)^T \cdot \mathbb{A}_{iN} \cdot \mathbb{J}_{CB}^N \\ \vdots & \ddots & \vdots & \ddots & \vdots \\ \left(\mathbb{J}_{CB}^N\right)^T \cdot \mathbb{A}_{N1} \cdot \mathbb{J}_{CB}^1 & \cdots & \left(\mathbb{J}_{CB}^N\right)^T \cdot \mathbb{A}_{Nj} \cdot \mathbb{J}_{CB}^j & \cdots & \left(\mathbb{J}_{CB}^N\right)^T \cdot \mathbb{A}_{NN} \cdot \mathbb{J}_{CB}^N \end{bmatrix} \tag{10}$$

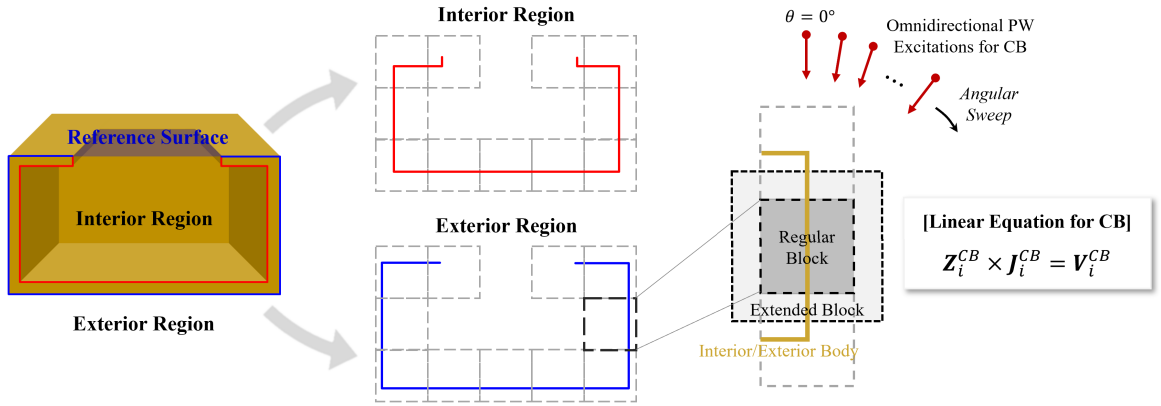

Fig. 2. Block generation of the open-ended cavity. The exterior and interior walls are divided into separate blocks. The CBFs are calculated by solving the linear equation in every block.

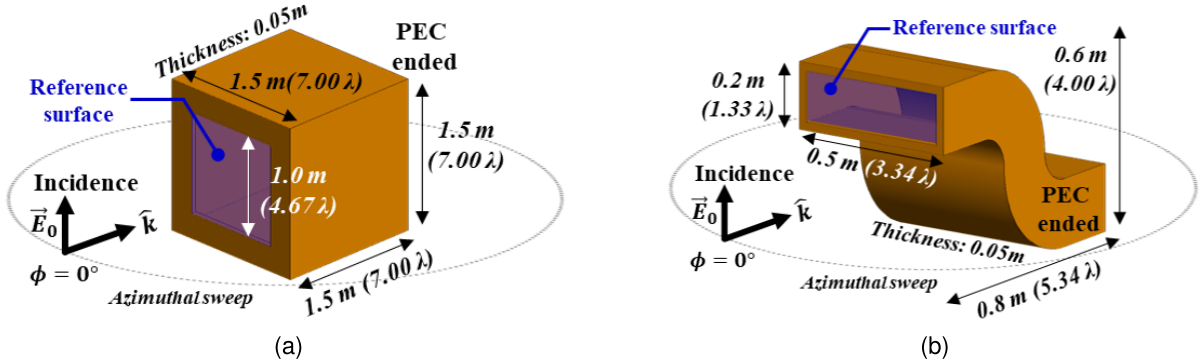

Fig. 3. Geometry and simulation configuration of (a) rectangular open-ended cavity and (b) S-shaped duct. The detailed dimension of the structures is described in the figure. The surface of the rectangular open-ended cavity is discretized by 77 780 triangular patches, generating 111 972 RWG basis functions. Moreover, the surface of the S-shaped duct is discretized by 74 346 triangular patches, generating 111 519 RWG basis functions. The reference surfaces of both examples consist of 4624 and 2519 RWG basis functions, respectively. The incident angle for excitation is swept azimuthally.

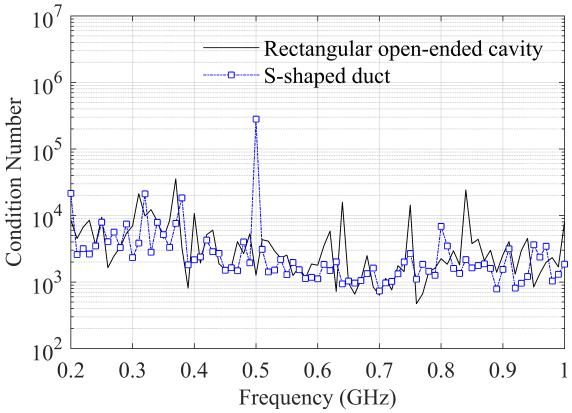

Fig. 4. Condition number versus frequency. The solid black line represents the data for the rectangular open-ended cavity, while the marked blue line represents the data for the S-shaped duct. Triangular meshes in both structures are generated at the highest frequency of 1.0 GHz and are identically used at lower frequencies.

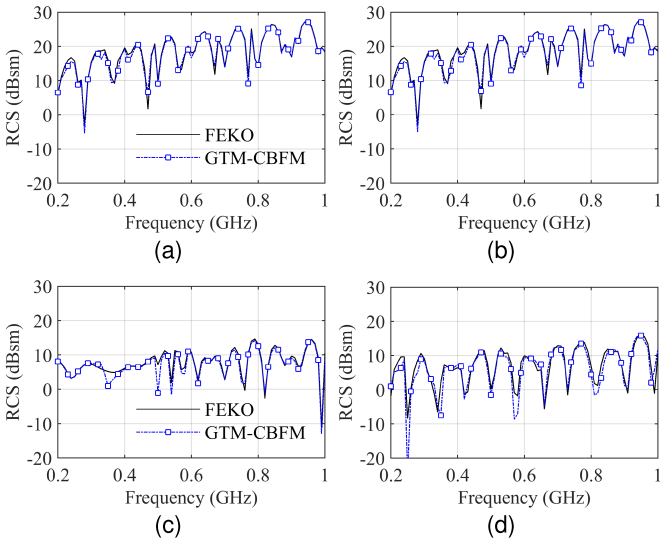

Fig. 5. Backscattered RCS results with respect to the frequency. (a) and (b) RCS results for HH- and VV-polarization of the rectangular open-ended cavity, respectively. (c) and (d) RCS results for HH- and VV-polarization of the S-shaped duct, respectively. The backscattered RCS is calculated in the facing direction perpendicular to the aperture plane.

where $\tilde{\mathbb{J}}_0$ represents the CBFs of the exterior wall and $\tilde{\mathbb{E}}_0^{inc}$ is the reduced excitation vector [19]. A solution to the problem can be obtained by solving (8), (9), (12), and (17). Consequently, the dimensions of the linear system are reduced compared to those of the original linear system, resulting in the reduction of the matrix-solving time.

IV. Numerical Simulation Results

In this section, we analyze two types of open-ended cavity structures. The first one is a rectangular cavity, and the second one is an S-shaped duct, as shown in Fig. 3. The results obtained from the simulation were compared with those obtained using Altair FEKO, the commercial software based on the MoMs. All simulations were performed using a workstation that operates with an Intel Xeon Gold 6444Y CPU @3.60 GHz.

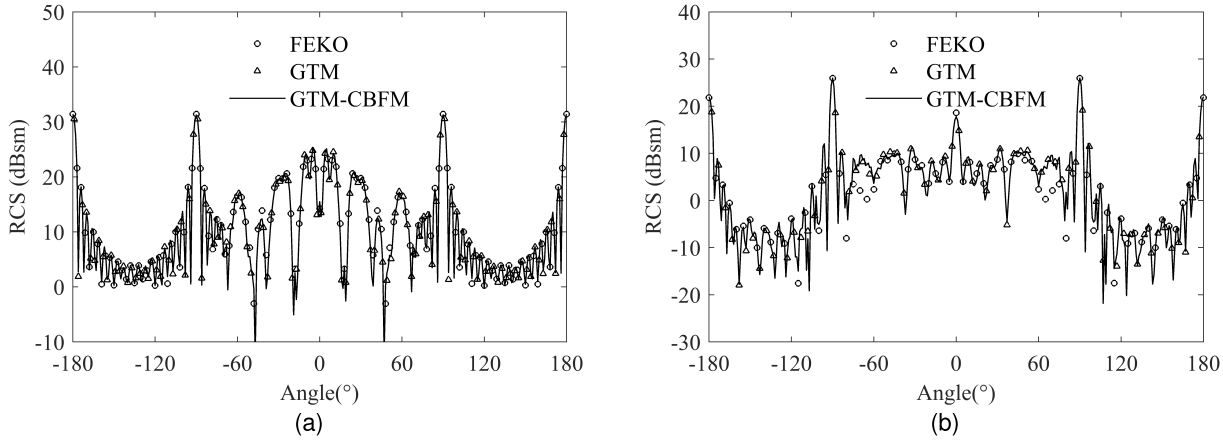

Fig. 6. Comparison of the monostatic RCS results of (a) rectangular open-ended cavity and (b) S-shaped duct at VV-polarization.

TABLE I
COMPARISON OF UNKNOWN INFORMATION AND COMPUTING TIME BETWEEN THE CONVENTIONAL AND PROPOSED METHODS

Index		Unknowns		Computation Time (sec.)				
		RWGs	CBFs	CBF generation	GTM model construction	System matrix formulation	Matrix solving	Total
Rectangular cavity	GTM	111,972	-	-	1,164.37	898.2	203.76	2,266.33
	GTM-CBFM	4,624	53,980	4.59	296.51	283.37	28.63	608.51
S-shaped duct	GTM	114,038	-	-	859.55	659.13	178.05	1,696.73
	GTM-CBFM	2,519	56,992	5.32	205.53	204.27	30.75	440.55

A. Numerical Stability

Numerical stability is a critical metric in numerical analysis algorithms. Poor numerical stability can lead to reduced convergence or accuracy of solutions. One method of evaluating numerical stability is by computing the condition number of matrices. Generally, in problems where numerical stability is poor, known as ill-conditioned problems, the condition number can be calculated to be a very large number. In our paper, we combine (8), (9), (12), (17) into a single matrix equation to obtain solutions, and we compute the distribution of condition numbers for the matrices obtained by scaling frequencies, as shown in Fig. 4. Due to the computational burden, the surfaces of the structures are discretized at a relatively lower frequency than the practical operating frequency. The triangular meshes in the rectangular open-ended cavity are generated at the highest frequency of 1.0 GHz and are identically used at lower frequencies, with the geometry divided into 0.5λ-sized blocks for CBFM at each frequency. Similarly, the triangular meshes in the S-shaped duct are generated at the highest frequency of 1.0 GHz and are identically used at lower frequencies, with the geometry also divided into 0.5λ-sized blocks. Mostly all of the values are below 10^6, indicating that the matrices are well-conditioned. To evaluate the accuracy of the solution, we calculated the backscattered RCS with respect to the frequency, as shown in Fig. 5. The backscattered RCS is calculated in the facing direction perpendicular to the aperture plane. According to the results, all RCS values have excellent agreement with FEKO. Therefore, it can be concluded that the convergence and accuracy of solutions are ensured.

B. Rectangular Open-Ended Cavity

The width, length, and height of the rectangular open-ended cavity are 7.0λ, as depicted in Fig. 3(a). The aperture size is 4.67λ by 4.67λ, which serves as the reference surface. The simulation is performed at a frequency of 1.4 GHz. The interior and exterior walls are divided into 988 and 1097 blocks, respectively, with each block having a size of 0.5λ. We used the result from [26] to decide the appropriate size of blocks for dividing the whole geometry

$$L_B^{opt} \approx 0.05 \times (N_{RWG})^{\frac{6}{29}} \tag{18}$$

where N_{RWG} is the number of RWGs in the geometry. When $N_{RWG} = 110\,000$, then $L_B^{opt} \approx 0.55$. We choose the block size as (1/2)λ, or 0.5λ, for simplicity. The value of the block size is also used for the other example. The blocks are extended by 0.1λ when calculating the CBF. The total numbers of generated CBFs are 28 867 and 25 113 on the exterior and interior walls, respectively. More detailed information for unknown variables is presented in Table I. The monostatic RCS results are compared in Fig. 6(a). The RCS results obtained from the commercial full-wave software, FEKO, are used as the reference data for validation, and all results exhibited excellent agreement. The computation times are tabulated and compared in Table I. As shown in the table, the proposed method significantly reduces the computational time. As expected, the computing time for GTM model construction is reduced by 40.3%, and the total computing time is reduced by 49.4%. Additionally, the simulation time using FEKO was recorded as 2774 s, indicating the superior computational performance of the proposed method.

C. S-Shaped Duct

The size of the S-shaped duct is 4.0λ × 3.34λ × 5.34λ, as shown in Fig. 3(b). The aperture dimensions are 1.33λ × 3.34λ, and it served as the reference surface. The simulation is carried out at a frequency of 2.0 GHz. The exterior and interior walls are divided into 1212 and 1041 blocks, respectively. The size of each block is 0.5λ. As in the

previous example, the blocks are extended by 0.1λ when calculating the CBF. The total numbers of generated CBFs are 31 492 and 25 500 on the exterior and interior walls, respectively. Detailed information for the unknown variables is presented in Table I. The comparison of monostatic RCS is depicted in Fig. 6(b), revealing almost perfect agreement. As presented in the table, the computation time is significantly reduced. The computing time for GTM model construction is reduced by 66.5%, and the total computing time is reduced by 65.9%. Additionally, the simulation time using FEKO was recorded as 2846 s, indicating the superior computational performance of the proposed method.

V. Conclusion

This study proposes a novel method for accelerating the performance of the GTM model for scattering problems of electrically large-scale open-ended cavities. The original unknowns for the electrical surface current on both the interior and exterior walls are represented by the lower number of CBFs. Various matrices in the GTM formulation are replaced with the reduced form using CBFs, which reduces the construction time for the GTM model. In addition, the linear system with the GTM model can be represented by the reduced form by using the CBFs, resulting in the reductions of both matrix formulation and solving time. To validate the effectiveness of our proposed method, we conducted numerical simulations on various open-ended cavity structures. We compared the results obtained from the proposed method with those from the original method and the commercial simulation software (FEKO). The monostatic RCS results have excellent agreement with other methods. Notably, the computation time is significantly reduced compared with the original method.

References

[1] J. Chauveau, N. de Beaucoudrey, and J. Saillard, "Resonance behavior of radar targets with aperture: Example of an open rectangular cavity," *IEEE Trans. Antennas Propag.*, vol. 58, no. 6, pp. 2060–2068, Jun. 2010.

[2] T.-M. Wang, A. Cuevas, and H. Ling, "RCS of partially open cavities in the resonant region," in *Dig. Antennas Propag. Soc. Int. Symp.*, Jun. 1989, pp. 1038–1041.

[3] H. T. Anastassiu, "A review of electromagnetic scattering analysis for inlets, cavities, and open ducts," *IEEE Antennas Propag. Mag.*, vol. 45, no. 6, pp. 27–40, Dec. 2003.

[4] Y.-H. Noh, C.-S. Park, J.-G. Yook, W.-Y. Choi, and Y.-H. Jang, "Analysis for contribution of engine inlet structure to monostatic RCS of aircraft in the VHF band," in *Proc. IEEE Int. Symp. Antennas Propag. USNC/URSI Nat. Radio Sci. Meeting*, Jul. 2018, pp. 2335–2336.

[5] R. F. Harrington, *Field Computation by Moment Methods*. Wiley, 1993.

[6] J.-M. Jin, *The Finite Element Method in Electromagnetics*. Hoboken, NJ, USA: Wiley, 2015.

[7] F. Obelleiro-Basteiro, J. Luis Rodriguez, and R. J. Burkholder, "An iterative physical optics approach for analyzing the electromagnetic scattering by large open-ended cavities," *IEEE Trans. Antennas Propag.*, vol. 43, no. 4, pp. 356–361, Apr. 1995.

[8] R. J. Burkholder and T. Lundin, "Forward-backward iterative physical optics algorithm for computing the RCS of open-ended cavities," *IEEE Trans. Antennas Propag.*, vol. 53, no. 2, pp. 793–799, Feb. 2005.

[9] R. Hémon, P. Pouliguen, H. He, J. Saillard, and J.-F. Damiens, "Computation of EM field scattered by an open-ended cavity and by a cavity under radome using the iterative physical optics," *Prog. Electromagn. Res.*, vol. 80, pp. 77–105, 2008.

[10] Z. Peng and X.-Q. Sheng, "A flexible and efficient higher order FE-BI-MLFMA for scattering by a large body with deep cavities," *IEEE Trans. Antennas Propag.*, vol. 56, no. 7, pp. 2031–2042, Jul. 2008.

[11] F.-G. Hu and C.-F. Wang, "Preconditioned formulation of FE-BI equations with domain decomposition method for calculation of electromagnetic scattering from cavities," *IEEE Trans. Antennas Propag.*, vol. 57, no. 8, pp. 2506–2511, Aug. 2009.

[12] D. C. Ross, J. L. Volakis, and H. T. Anastassiu, "Hybrid finite element-modal analysis of jet engine inlet scattering," *IEEE Trans. Antennas Propag.*, vol. 43, no. 3, pp. 277–285, Mar. 1995.

[13] A. Zdunek and W. Rachowicz, "Efficient jet-engine inlet radar cross-section prediction using higher-order finite-element method and reduced-order modeling," *Electromagnetics*, vol. 34, nos. 3–4, pp. 345–362, Apr. 2014.

[14] J. Hu et al., "Domain decomposition method based on integral equation for solution of scattering from very thin, conducting cavity," *IEEE Trans. Antennas Propag.*, vol. 62, no. 10, pp. 5344–5348, Oct. 2014.

[15] S. Xiang, G. Xiao, and J. Mao, "A generalized transition matrix model for open-ended cavity with complex internal structures," *IEEE Trans. Antennas Propag.*, vol. 64, no. 9, pp. 3920–3930, Sep. 2016.

[16] Y. Hu, G. Xiao, and S. Xiang, "A generalized transition matrix model combined with discontinuous Galerkin method for open cavities," *IEEE Open J. Antennas Propag.*, vol. 1, pp. 272–282, 2020.

[17] S. Xiang, G. Xiao, X. Tian, and J. Mao, "Analysis of large-scale phased antenna array with generalized transition matrix," *IEEE Trans. Antennas Propag.*, vol. 61, no. 11, pp. 5453–5464, Nov. 2013.

[18] G. Xiao, J. Mao, and B. Yuan, "Generalized transition matrix for arbitrarily shaped scatterers or scatterer groups," *IEEE Trans. Antennas Propag.*, vol. 56, no. 12, pp. 3723–3732, Dec. 2008.

[19] V. V. S. Prakash and R. Mittra, "Characteristic basis function method: A new technique for efficient solution of method of moments matrix equations," *Microw. Opt. Technol. Lett.*, vol. 36, no. 2, pp. 95–100, Jan. 2003.

[20] C.-S. Park, I.-P. Hong, Y.-J. Kim, and J.-G. Yook, "Acceleration of multilevel characteristic basis function method by multilevel multipole approach," *IEEE Trans. Antennas Propag.*, vol. 68, no. 10, pp. 7109–7120, Oct. 2020.

[21] I.-H. Kim, H.-R. Im, I.-P. Hong, Y.-J. Kim, and J.-G. Yook, "CBF computation acceleration of CBFM using k-Means clustering algorithm," *J. Korean Inst. Electromagn. Eng. Sci.*, vol. 33, no. 12, pp. 926–930, Dec. 2022.

[22] H.-R. Im, W. Kim, Y.-H. Noh, I.-P. Hong, and J.-G. Yook, "RCS estimation of singly curved dielectric shell structure with PMCHWT method and experimental verification," *Sensors*, vol. 22, no. 3, p. 734, Jan. 2022.

[23] I. Kim, H.-R. Im, I.-P. Hong, H. Lee, and J.-G. Yook, "Generalized transition matrix model using characteristic basis function method for open-ended cavities," in *Proc. 18th Eur. Conf. Antennas Propag. (EuCAP)*, Mar. 2024, pp. 1–3.

[24] W. C. Gibson, *The Method of Moments in Electromagnetics*. Boca Raton, FL, USA: CRC Press, 2021.

[25] K. Zhao, M. N. Vouvakis, and J.-F. Lee, "The adaptive cross approximation algorithm for accelerated method of moments computations of EMC problems," *IEEE Trans. Electromagn. Compat.*, vol. 47, no. 4, pp. 763–773, Nov. 2005.

[26] C.-S. Park, Y.-R. Jeong, I.-P. Hong, and J.-G. Yook, "Block size optimization of CBFM for scattering problems," *IEEE Trans. Antennas Propag.*, vol. 66, no. 10, pp. 5370–5377, Oct. 2018.